

Provided for non-commercial research and education use.  
Not for reproduction, distribution or commercial use.



This article appeared in a journal published by Elsevier. The attached copy is furnished to the author for internal non-commercial research and education use, including for instruction at the authors institution and sharing with colleagues.

Other uses, including reproduction and distribution, or selling or licensing copies, or posting to personal, institutional or third party websites are prohibited.

In most cases authors are permitted to post their version of the article (e.g. in Word or Tex form) to their personal website or institutional repository. Authors requiring further information regarding Elsevier's archiving and manuscript policies are encouraged to visit:

<http://www.elsevier.com/copyright>



Contents lists available at ScienceDirect

Physics Letters A

www.elsevier.com/locate/pla



## Thermal transport in multiwall carbon nanotube buckypapers

Yanan Yue, Xiaopeng Huang, Xinwei Wang\*

Department of Mechanical Engineering, 2025 Black Engineering Building, Iowa State University, Ames, IA 50011-2161, USA

### ARTICLE INFO

#### Article history:

Received 8 April 2010

Received in revised form 18 June 2010

Accepted 12 August 2010

Available online 17 August 2010

Communicated by R. Wu

### ABSTRACT

A steady-state electro-Raman-thermal (SERT) technique is developed to characterize the thermal transport in multiwall carbon nanotube (MWCNT) buckypapers. This SERT technique involves steady-state joule heating of a suspended sample and measuring its middle point temperature based on Raman shift intensity. The thermal conductivity is determined from linear fitting of the temperature against heating power. Combined with the transient-electro-thermal technique, the thermophysical properties of two MWCNT buckypapers are characterized as 1.19 and 2.92 W/(mK) for thermal conductivity,  $3.65 \times 10^{-6}$  and  $7.58 \times 10^{-6}$  m<sup>2</sup>/s for thermal diffusivity, 459 and 543 kg/m<sup>3</sup> for density. Detailed discussion and analysis are provided about the uncertainty of the SERT technique and its capacity for measuring wires down to sub- $\mu$ m length. The low thermal conductivity of the buckypaper indicates its thermal transport is determined by the thermal contact resistance between MWCNTs. These contact points feature low thermal conductance. The mean distance between two adjacent contact points is estimated in the order 45–450  $\mu$ m and 93–933  $\mu$ m for the two samples, indicating low-density contacts within the buckypaper.

© 2010 Elsevier B.V. All rights reserved.

### 1. Introduction

As the promising material in micro-electro-mechanical systems (MEMS) and nano-electro-mechanical systems (NEMS), one-dimensional micro/nanoscale materials such as carbon nanotubes (CNTs), are attracting significant interest for their superior mechanical and electrical characteristics. Extensive work has been devoted for characterizing their thermophysical properties which are tightly related to their structure and are important for their industrial applications. Several non-contact techniques have been established successfully on thermal transport study of micro/nanoscale materials: the  $3\omega$  method, the microfabricated device method, the optical heating electrical thermal sensing (OHETS) technique, the transient electrothermal (TET) technique, the transient photo-electrothermal (TPET) technique, and the pulsed laser-assisted thermal relaxation (PLTR) technique [1–8].

These techniques have great capacity for thermophysical property characterization of micro/nanowires while each of them has certain limitations. Physically, the  $3\omega$  method detects the  $3\omega$  signal in the specimen during the self-joule heating to study the resistance change, which is used to determine thermal diffusivity [1]. Despite its simple experimental principle, the  $3\omega$  technique suffers from poor signal to noise ratio and is vulnerable to various noises in the power source and environment. The OHETS method

tracks the temperature evolution and phase shift difference between temperature and laser beam during under periodical laser heating. This technique overcomes the drawback of the  $3\omega$  method and features significantly improved signal-to-noise ratio and ease of experiment conduction. The experimental time of this technique is much shorter than that of the  $3\omega$  method [4]. The other three techniques like TET, TPET and PLTR probe the temperature evolution during step electrical/laser heating or after pulsed laser heating to evaluate the thermal diffusivity. The time required for these three techniques is significantly shorter than that for the  $3\omega$  and OHETS techniques. In these three transient techniques, the thermal relaxation time of the sample is  $\sim l^2/\alpha$ , where  $l$  is the sample length and  $\alpha$  is its thermal diffusivity. For samples of very short length and high thermal diffusivity, the characteristic heat transfer time would be very short and it becomes difficult to employ the transient techniques. Besides, all the techniques reviewed above have no capacity for direct temperature measurement, which is a critical requirement for analyzing the heat transfer process in materials and determining thermal conductivity [5–8].

To overcome the challenges mentioned above, the Raman spectroscopy is adopted in this work for temperature measurement and heat transfer analysis. Based on the Raman spectra's dependence on temperature, Raman thermometry is a compelling technique for non-contact temperature probing and has been applied successfully on the silicon and CNTs analysis [9–12]. For the particular structure of CNTs, there are three vibration modes which appear as three peaks in the Raman spectrum within the Raman shift range from 100 cm<sup>-1</sup> to 2000 cm<sup>-1</sup>: radial breathing

\* Corresponding author. Tel.: +1 515 294 2085; fax: +1 515 294 3261.  
E-mail address: xwang3@iastate.edu (X. Wang).

mode (RBM), disorder induced D-band and graphite-related optical mode (G-band) [13,14]. In these peaks, D-band and G-band at about  $1300\text{ cm}^{-1}$  and  $1600\text{ cm}^{-1}$  are often taken to analyze due to their distinct feature. In Raman thermometry, two approaches can be used for temperature measurement due to the temperature dependence of the Stokes effect. First, the Raman frequency shows downshift character as the temperature increases [15–18]. Therefore, different temperatures can be distinguished by studying different peak positions. However, one noticeable disadvantage of this method applying to the CNT is its low sensitivity [17]. For example, the temperature coefficient of G-band frequency is as low as  $-1.67 \times 10^{-5}\text{ K}^{-1}$  [15]. Moreover, defining the peak position precisely is very difficult if the peak is not very sharp (e.g. for MWCNTs). It often requires Raman spectrometers with considerably high resolution in order to realize even medium temperature resolution. The other approach for temperature sensing is based on the character that Raman peak intensity changes with temperature significantly. This is an intrinsic property of many materials, such as silicon. CNTs also have this feature, which is found that the intensity of peaks at either D-band or G-band will decrease as the temperature goes up [16,19,20]. Moreover, the sensitivity of this intensity-based approach is much higher than that of frequency based method. Due to the difference of the decreasing rate of D-band and G-band, the height ratio of these two peaks is also temperature dependant. In Z.H. Ni et al.'s work, the ratio of D-band to G-band peaks decreases by almost 50% as the temperature increase as high as  $900^\circ\text{C}$ , but changes slightly if the temperature does not increase enough [19]. We would not use this ratio-based method because of the low temperature rise in our experimental setup. Considering all strengths and weaknesses of the aforementioned two methods, intensity-based method is more appealing for application, especially when the spectrum is not sharp and only small temperature rise is present in the experiment. Based on the Raman thermometry, recently we have developed a steady-state electro-Raman-thermal (SERT) technique, which can directly measure the temperature of micro/nanowires under steady-state joule heating. Furthermore, the combined steady-state electric heating and temperature measurement based on the Raman spectroscopy lead to direct characterization of the thermal conductivity of the sample [21].

In this work, we report on a systematic study of thermal transport in multiwall CNT (MWCNT) buckypapers, whose thermal conductivity is determined by the numerous contacts between MWCNTs. Section 2 details the experimental principles and physical models used in the SERT technique, and Section 3 presents the experimental details and results. Discussions are given about the experimental uncertainty and the number density of MWCNT contacts within the buckypaper.

## 2. Experimental principle and physical model development

### 2.1. Experimental principle

There are two stages involved in the SERT technique: calibration and thermal characterization. At the calibration stage, the sample is attached to a heating plate whose temperature is controlled constant and uniform. The sample and the plate are close enough to be considered at the same temperature. The Raman signal from the sample is measured at different temperatures. Accordingly, the relationship between the Raman signal (peak intensity) and the temperature can be established. In thermal characterization, the wire-like sample is suspended between two electrodes as shown in Fig. 1(a). The DC power is applied on the sample to induce the electric heating. According to the one-dimensional heat transfer equation, the highest temperature is located at the middle point of the sample and this temperature is closely determined by the

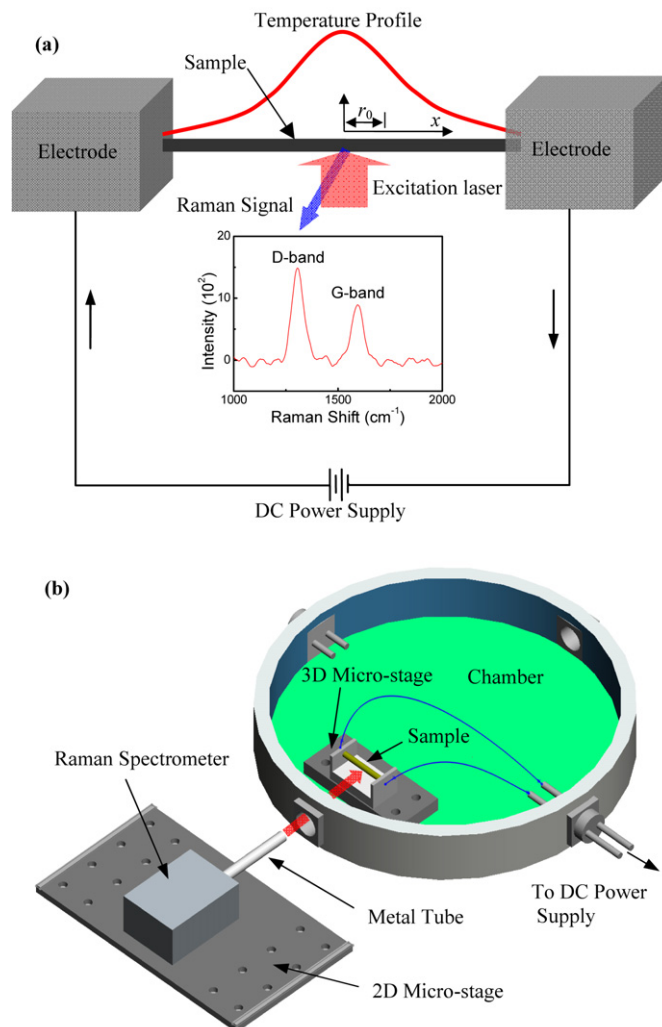


Fig. 1. (a) Schematic of the experimental principle for the SERT technique; (b) schematic of experimental setup (not to scale).

thermal conductivity and the input power. The same laser used in the calibration stage is employed to excite the sample for Raman spectroscopy to monitor its temperature evolution. Once the relationship between temperature and input DC heating power is obtained, the thermal conductivity can be calculated by linear fitting. The SERT technique also considers the heating effect induced by the probing laser and explores a feasible approach to measuring the thermal conductivity of wires at micro/nanoscales.

### 2.2. Physical model development

As shown in Fig. 1(a), a conductive micro/nanowire of length  $2L$  is suspended between two electrodes with its axial direction defined as the  $x$  direction and  $x = 0$  is located at the middle point of sample. The probing laser with a spot size of  $2r_0$  in diameter is uniformly distributed along the wire with the absorbed energy per unit volume as  $\dot{Q}_p = Q_p / (A_c \cdot r_0)$ , where  $Q_p$  is total absorbed photon energy,  $A_c$  is the cross-sectional area of the sample. The DC current  $I$  is passed through the sample to induce a steady-state joule heating as  $\dot{Q}_e = I^2 R / (A_c \cdot L)$ , where  $R$  is the sample's resistance. Under the circumstance that the wire is placed in a vacuum, only heat conduction along the wire is significant, while heat convection and thermal radiation from the wire are negligible. Considering the temperature effect on the thermal conductivity of CNTs, the Umklapp phonon-phonon scattering will

give  $1/T$  temperature dependence and the three-phonon scattering will contribute second order dependence. The thermal conductivity changes with temperature in the format of  $1/(\alpha T + \beta T^2)$  [22–25]. If the temperature increase is at low scale from the room temperature, lower than 100 K for example, only the first order term gives significant effect [26]. Meanwhile, the nanotubes are twisted in the buckypaper, leading to relatively high contact resistance between two CNTs. In addition, due to the strong suppression of the interface transmission, the temperature dependence of interface thermal conductance is much weaker than that of the single nanotube at low temperatures above 100 K [27]. With all these factors considered, the conductivity can be deduced in the form of  $\alpha/(T + \beta)$ , where  $\alpha$  and  $\beta$  are constants. The temperature of the wire in the range of  $x = 0$  to  $r_0$  can be derived as:

$$T(x) = (T_0 + \beta) \cdot \exp\left(-\frac{\dot{Q}_e + \dot{Q}_p}{2\alpha} x^2\right) - \beta \quad (0 < x < r_0). \quad (1)$$

In addition, the relationship between the middle point temperature ( $T_0$ ) and the end point temperature ( $T_L$ ) is expressed as:

$$T_0 = (T_L + \beta) \cdot \exp\left(-\frac{\dot{Q}_p}{2\alpha} r_0^2 + \frac{\dot{Q}_e}{2\alpha} L^2 + \frac{\dot{Q}_p}{\alpha} r_0 \cdot L\right) - \beta. \quad (2)$$

Therefore, the average temperature of the laser irradiation area on the sample is expressed as:

$$\begin{aligned} \bar{T}_r = & (T_L + \beta) \cdot \exp\left(-\frac{\dot{Q}_p}{2\alpha} r_0^2 + \frac{\dot{Q}_e}{2\alpha} L^2 + \frac{\dot{Q}_p}{\alpha} r_0 \cdot L\right) \\ & \cdot \frac{1}{2r_0} \sqrt{\frac{2\pi\alpha}{\dot{Q}_p + \dot{Q}_e}} \cdot \operatorname{erf}\left(r_0 \sqrt{\frac{\dot{Q}_p + \dot{Q}_e}{2\alpha}}\right) - \beta. \end{aligned} \quad (3)$$

At the calibration stage, no electric heating is applied on the sample and only laser heating effect is involved. The average temperature of the laser irradiation area ( $\bar{T}_{r,c}$ ) should be

$$\begin{aligned} \bar{T}_{r,c} = & (T_L + \beta) \cdot \exp\left(-\frac{\dot{Q}_p}{2\alpha} r_0^2 + \frac{\dot{Q}_p}{\alpha} r_0 \cdot L\right) \\ & \cdot \frac{1}{2r_0} \sqrt{\frac{2\pi\alpha}{\dot{Q}_p}} \cdot \operatorname{erf}\left(r_0 \sqrt{\frac{\dot{Q}_p}{2\alpha}}\right) - \beta. \end{aligned} \quad (4)$$

In this equation, the end point's temperature ( $T_L$ ) is considered the same as the heating plate temperature and the latter is much easier to measure. The heating plate temperature ( $T_L$ ) is recorded at the calibration stage in the experiment. Since the temperatures in the measurement experiment ( $T_m$ ) are deduced from the calibration result, the real measured temperature should be:

$$\begin{aligned} \bar{T}_r = & (T_m + \beta) \cdot \exp\left(-\frac{\dot{Q}_p}{2\alpha} r_0^2 + \frac{\dot{Q}_p}{\alpha} r_0 \cdot L\right) \\ & \cdot \frac{1}{2r_0} \sqrt{\frac{2\pi\alpha}{\dot{Q}_p}} \cdot \operatorname{erf}\left(r_0 \sqrt{\frac{\dot{Q}_p}{2\alpha}}\right) - \beta \\ = & (T_L + \beta) \cdot \exp\left(-\frac{\dot{Q}_p}{2\alpha} r_0^2 + \frac{\dot{Q}_e}{2\alpha} L^2 + \frac{\dot{Q}_p}{\alpha} r_0 \cdot L\right) \\ & \cdot \frac{1}{2r_0} \sqrt{\frac{2\pi\alpha}{\dot{Q}_p + \dot{Q}_e}} \cdot \operatorname{erf}\left(r_0 \sqrt{\frac{\dot{Q}_p + \dot{Q}_e}{2\alpha}}\right) - \beta. \end{aligned} \quad (5)$$

In the electrical heating measurement experiment, the end point is assumed to be constant at room temperature ( $T_L = T_\infty$ ) because the connecting electrodes are excellent heat sinks compared with the sample. In the measurement, the electric heating power and the laser heating power is comparable, the electric

heating power density should be much smaller than the laser heating power density ( $\dot{Q}_e \ll \dot{Q}_p$ ) because the length of the wire is much longer than the spot size. As a consequence, the terms  $\sqrt{\frac{2\pi\alpha}{\dot{Q}_p + \dot{Q}_e}} \cdot \operatorname{erf}\left(r_0 \sqrt{\frac{\dot{Q}_p + \dot{Q}_e}{2\alpha}}\right)$  and  $\sqrt{\frac{2\pi\alpha}{\dot{Q}_p}} \cdot \operatorname{erf}\left(r_0 \sqrt{\frac{\dot{Q}_p}{2\alpha}}\right)$  can be cancelled out, and Eq. (5) can be simplified as

$$T_m = (T_\infty + \beta) \cdot \exp\left(\frac{\dot{Q}_e \cdot L^2}{2\alpha}\right) - \beta. \quad (6)$$

In addition, the correlation of  $T_m$  and  $T_\infty$  can be considered as linear relationship if the heating power density starts at 0, that is  $T_m = \dot{Q}_e \cdot L^2 (T_\infty + \beta) / 2\alpha + T_\infty$ . Substituting  $k = \alpha / (T + \beta)$  and  $\dot{Q}_e = I^2 R / (A_c \cdot L)$  into this equation, the relationship between measured temperature and the electric heating power is established as  $T_m = P \cdot L / (4k \cdot A_c) + T_\infty$ , where  $P$  is the input electric power  $I^2 R$ ,  $k$  is the thermal conductivity at room temperature. Theoretically, the thermal conductivity of the sample can be determined by the linear fitting of the relationship between  $T_m$  and  $P$ .

### 3. Experimental details and results

#### 3.1. Experimental setup

The diversity of fabrication method and conditions for CNTs make them have different Raman spectrum characteristics (peak position, intensity and width) due to the different intrinsic particular structures in the bundle. In addition, different probing sources (laser with different wavelengths) may affect the spectrum character a lot [28]. The MWCNT samples used in this experiment are pieces of buckypaper purchased from Nanolab Inc. In the buckypaper, the hollow structured MWCNTs were bonded together using a dispersion agent-Surfynol CT-131 Grind Aid manufactured by Air Products. This buckypaper can be folded and cut for different purposes. Our samples are pieces cut from the buckypaper with purity of CNTs at 95%, which ensures sound Raman signal. More details about the sample would be discussed together with the results in the next section. A BTC162 high resolution TE Cooled CCD Array spectrometer from BWTek Inc. is employed to detect the Raman signal. A polarized probing laser installed in front of the spectrometer has a spot size around 160  $\mu\text{m}$ , wavelength of 784.2 nm and 62 mW power output.

In the calibration, the sample is attached on a heater using silver paste. The heater's temperature is monitored by using a T type thermocouple with 0.13 mm diameter. The thermocouple is placed close enough to the sample to make the temperature measurement accurate. The temperature values are controlled by a PTC 10 programmable temperature controller from Stanford Research Inc. with an uncertainty less than 1 °C. The temperature is increased evenly from room temperature to 110 °C, and several Raman spectra are recorded with 60 s integration time when the temperature value reaches steady state.

The measurement experiment is conducted in a vacuum chamber with pressure below  $1 \times 10^{-3}$  Torr. The system schematic is shown in Fig. 1(b). The MWCNT buckypaper is suspended between two copper electrodes on a sample holder with two ends attached by silver paste. The sample holder is on a 3D micro-stage with electrodes connected to the electrical feedthrough of the chamber. The electrical current comes from a Model 6221 power source (Keithley Inc.) for the DC current in the SERT experiment and square-wave current in the TET experiment. As shown in the figure, the Raman spectrometer is also on a 2D micro-stage and is located in front of the quartz window of the chamber. The laser beam from the probing metal tube passes through the quartz window and focuses on the middle point of the sample. In the

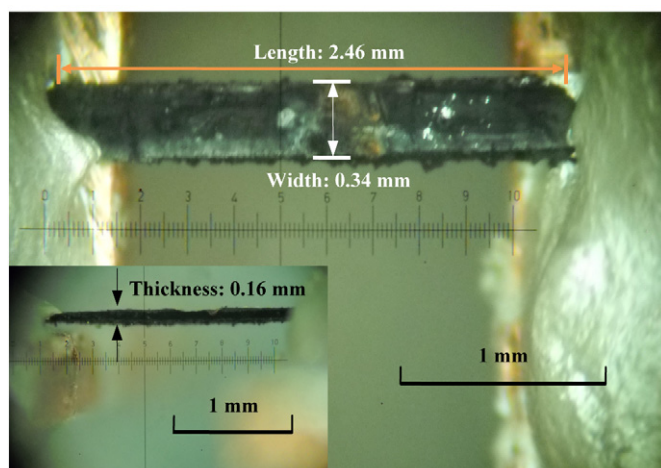


**Fig. 2.** Picture of Sample 1 observed under optical microscope. The sample measures 2.46 mm, 0.34 mm, and 0.16 mm in length, width, and thickness, respectively.

experiment, positions of both the sample and the Raman spectrometer can be adjusted by the micro-stages to meet the focus requirement of the laser and to position the laser in the middle of the sample. Since the focal length of the excitation laser is only 6 mm, which includes the thickness of the quartz window, the alignment of the system is the most critical part in the whole experiment. Especially when the chamber is under vacuum, the quartz window would be distorted by the great strength of pressure differential over it, and then the optical path is distorted accordingly. In the experiment, after the sample is placed in the vacuum chamber and before the lid is placed, the optical alignment is conducted to make sure the excitation laser beam is focused on the middle of the sample and sound Raman signal is obtained. Then after the chamber is vacuumed, the 2D micro-stage outside the chamber is used for fine-adjustment to ensure sound Raman signal.

In the experiment, the electrical current is controlled to increase with larger steps at low values and smaller steps at high values up to 20 mA. As the pressure in the chamber decreases below  $1 \times 10^{-3}$  Torr, the density of air has reduced to a quite low level and the mean free path of air molecules has increased to a few centimeters long. Therefore, the Fourier's law of heat conduction is not applicable for use in this case [1]. The heat conduction effect from the sample surface to the adjacent air can be neglected. Only heat conduction along the axial direction of the sample is considered during the steady-state electrical heating. Therefore, the physical model described in the previous section is applicable for this experiment.

### 3.2. Calibration experiment

In this work, thermal characterization is conducted on MWCNT buckypapers of two samples. The dimensions of Sample 1 are 2.46 mm, 0.34 mm and 0.16 mm in length, width and thickness, respectively. Its electrical resistance is 40.2  $\Omega$ . The picture of Sample 1 is shown as Fig. 2. The thickness is calculated from the average of several positions on the cross-section of the sample. Selected spectra obtained from calibration experiment at different temperatures are shown in Fig. 3(a). The peak of D-band is preferred for analyzing because it is sharper and has higher intensity than the G-band. In addition, the spectra obtained from this experiment are smoother than those we measured before using other kind of CNTs [21]. The relationship between normalized peak intensity ( $I^*$ ) and temperature  $T_L$  is established and shown in Fig. 3(b). It is noticed that the normalized intensity re-

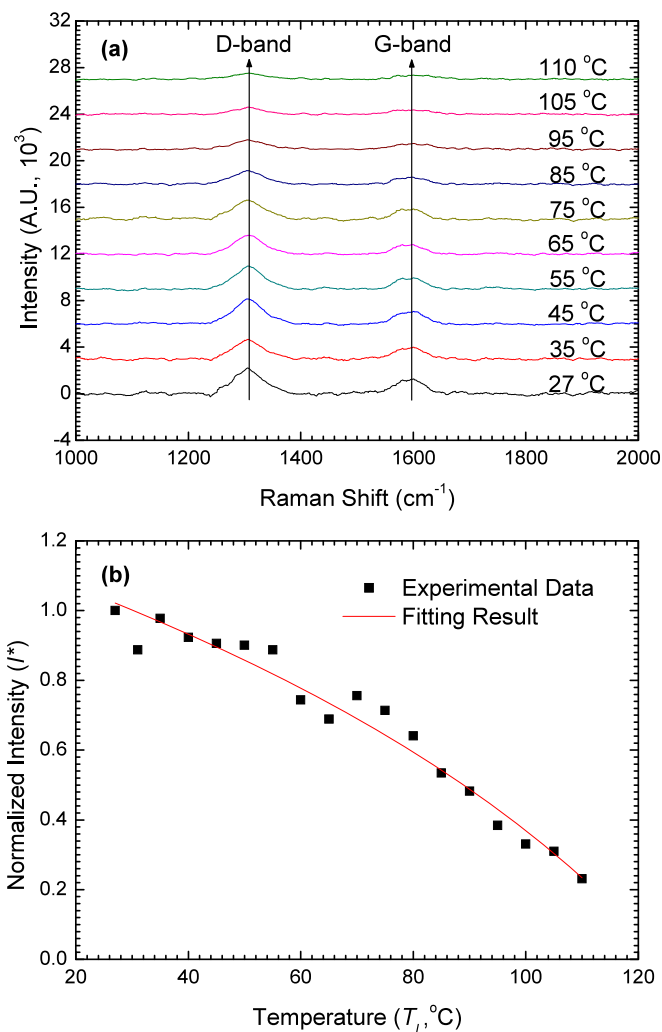


**Fig. 3.** (a) Spectra at different temperatures in the calibration; (b) the correlation between normalized peak height of the D-band and temperature. The experimental data is fitted with a logarithm function  $I^* = \ln(3.27 - 0.018T_L)$  with  $I^*$  being the normalized intensity with respect to that at room temperature.

duces by more than 70% of the initial value when the temperature increases from room temperature to about 110 °C. The correlation between them is fitted well with a logarithm function of  $I^* = \ln(3.27 - 0.018T_L)$ . This fitted curve will be used in the thermal characterization stage for temperature evaluation.

Our calibration result shows difference from those by other researchers. For example, Chiashi et al. [20] obtained an exponential relationship between temperature and the intensity of the G-band for single-wall CNTs (SWCNTs), which have much lower temperature coefficient than our measurement result. There are three possible reasons for this difference. First, the structure difference between MWCNT and SWCNT could result in the difference in Raman spectrum and their dependence on temperature. Second, the vibration modes of G-band and D-band are totally different, which leads to the different temperature dependence of these two bands. For the SWCNT sample, the G-band intensity is often higher than the D-band, while the D-band intensity is higher than the G-band for the MWCNT bundle in this experiment. Finally, the laser sources used in their experiment (Ar ion laser with wavelengths of 488.0 and 514.5 nm and a He-Ne laser with wavelength of 632.8 nm) are different from ours (784.2 nm). The measured Raman spectrum could have some difference because of the different power of the laser. To prove this, we take the measurement of the same sample on a confocal Raman spectrometer with wavelength of 532 nm

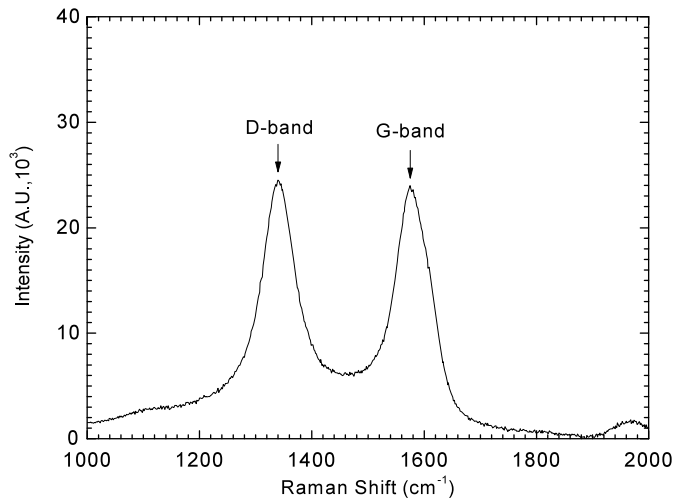


**Fig. 4.** The Raman spectrum using a confocal Raman spectrometer with wavelength of 532 nm, 20 mW energy and 10 s integration time.

and power of 20 mW. The result is shown in Fig. 4. It is found that the signal of the D-band and G-band is better than the result of our portable Raman system used in this experiment. The Raman spectrum is not only dependent on the wavelength and energy of the excitation laser, but also related to the quality of the sample. As the D-band is called defect-induced mode which indicates the defect of the CNT's structure, the higher the ratio of peak of the D-band to that of the G-band, the lower is the quality of the CNTs [29]. As shown in Fig. 4, the peaks of the D-band and G-band measured by the confocal Raman spectrometer are comparably high. In Fig. 3(a), the D-band is even stronger than the G-band, which shows that our CNT samples have high level of structure defect. Since both the sample quality and the probing source can affect the Raman spectrum, the temperature coefficient of Raman spectrum should be characterized individually when analyzing different kinds of CNT samples.

### 3.3. Thermal characterization of MWCNT buckypaper

In the measurement, several spectra are collected at different electrical currents from 0 to 20 mA and the Raman peak intensity of D-band is normalized with respect to the spectrum without electrical heating. According to the established relationship between the normalized intensity and temperature in the calibration, the corresponding temperatures of different spectra are determined by evaluating the peak intensity of D-band. The correlation between temperature and input electrical power is obtained and shown in Fig. 5. Their relationship is linearly fitted well. Considering the function of the middle point temperature  $T_m = P \cdot L / (4k \cdot A_c) + T_\infty$  and applying the fitted value of the slope  $L / (4k \cdot A_c)$ , the thermal conductivity ( $k$ ) of the MWCNT buckypaper (Sample 1) is calculated as 1.19 W/(mK).

To verify the strong capacity of the SERT technique, another MWCNT buckypaper (Sample 2) with 5.51 mm, 2.22 mm and 0.16 mm in length, width and thickness and 8.0  $\Omega$  resistance is also measured under the same condition. Its thermal conductivity is measured as 2.92 W/(mK). The difference in the thermal conductivity can be induced by the different bundle patterns of CNTs in the sample. In this work, the thermal diffusivity is also measured for these two samples using the TET technique developed by our group [5]. Due to the relationship between thermal conductivity and thermal diffusivity, the density of these two samples can be calculated and used to evaluate their structure variation from sample to sample.

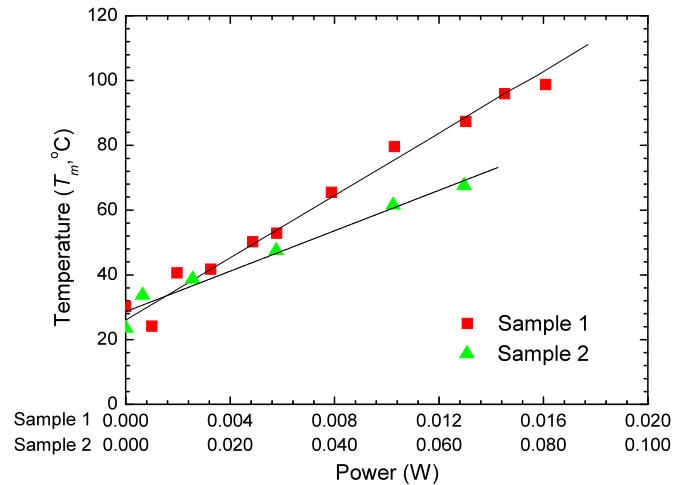


**Fig. 5.** The relationship between temperature and heating power. The solid black lines are the linear fitting of the experimental data (blocks and triangles).

In the TET technique, the sample is also suspended between two copper electrodes and the two ends are glued with silver paste to reduce both thermal and electrical contact resistances. The sample is housed in a vacuum chamber with the pressure below  $1 \times 10^{-3}$  Torr to make the heat convection negligible. An electrical heating through the sample is induced by applying a step DC current. The heating will cause temperature evolution of the sample at the beginning of the heating which is tightly related to the heat transfer along the sample. If the sample has a linear correlation, no matter positive or negative, between electrical resistance and temperature in a certain temperature range, the temperature evolution of the sample can be sensed by measuring the voltage evolution when the current is constant. Periodical electrical heating is applied with a square wave DC current. At the same time, the data of several periods of the experiment are recorded and the repeatability of this experiment can be evaluated. It should be mentioned that this period time of the square wave current should be chosen carefully to make sure the heat transfer process gets to the steady state after half period of heating and then go back to the initial state after another half period of no heating. Because it is a transient process, the current source should have very small rising time compared with the characteristic thermal transport time of the sample. In this experiment, the current supply Keithley 6221 with 2  $\mu\text{s}$  rising time is used. The voltage evolution is monitored and recorded by a Tektronix TDS7054 Digital Phosphor oscilloscope which has a maximum sampling rate of 5 GS/s. Consequently, the thermal diffusivity of the sample can be obtained by fitting the normalized temperature evolution curve against time with a robust program [5]. The measured normalized temperature evolution of Samples 1 and 2 and the global fitting results are shown in Fig. 6. The currents used in Sample 1 and Sample 2 are 20 mA and 25 mA, respectively. The period of the square wave is set to 10 s. Sound agreement is observed between the experimental data and theoretical fitting as shown in Fig. 6.

With the TET technique, the thermal diffusivity  $\alpha$  of Samples 1 and 2 is measured as  $3.65 \times 10^{-6} \text{ m}^2/\text{s}$  and  $7.58 \times 10^{-6} \text{ m}^2/\text{s}$ , respectively. Applying the previous thermal conductivity  $k$  values and the specific heat  $c_p$  of graphite 709 J/(kgK) at room temperature [30], the density  $\rho$  of the sample is calculated as 459  $\text{kg}/\text{m}^3$  and 543  $\text{kg}/\text{m}^3$  for Samples 1 and 2, respectively. The results show that Sample 2 has a thermal diffusivity much higher than that of Sample 1, explaining its higher thermal conductivity as measured by the SERT technique, while the density has no much difference. The experimental results discussed in this work are summarized in Table 1.

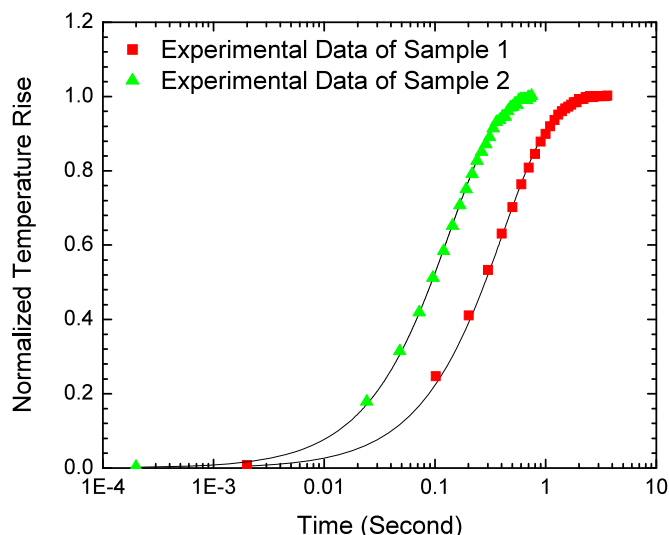


**Fig. 6.** The normalized temperature rise against time in the TET experiment. Solid lines are theoretical fitting results of the experimental data (blocks and triangles).

**Table 1**

Details of experimental results for the two MWCNT buckypapers.

	Sample 1	Sample 2
Length (mm)	2.46	5.51
Width (mm)	0.34	2.22
Thickness (mm)	0.16	0.16
Resistance ( $\Omega$ )	40.2	8.0
Thermal conductivity (W/(mK))	1.19	2.92
Thermal diffusivity ( $\text{m}^2/\text{s}$ )	$3.65 \times 10^{-6}$	$7.58 \times 10^{-6}$
Density ( $\text{kg}/\text{m}^3$ )	459	543

### 3.4. Results discussion

#### 3.4.1. Thermal conductivity analysis

The thermal conductivity and electrical conductivity of metals are closely related to each other because they are related to the same transport medium—electrons. However, for CNTs, the electrical conductivity comes from the movement of free electrons while the thermal conductivity is attributed to the phonon transport (lattice vibration). The Wiedemann–Franz Law relates the electrical conductivity ( $\sigma$ ) to the thermal conductivity ( $k$ ) by electrons:  $k/\sigma T \approx L_0$ , where  $L_0 = 2.45 \times 10^{-8} \text{ V}^2/\text{K}^2$ . The electrical conductivity  $\sigma$  can be calculated by the resistance and geometry of the sample [31]. From this equation, this thermal conductivity ( $k$ ) can be estimated to compare with our experimental values, which gives idea about the contribution of the heat carried by electrons [32]. Applying the data for Sample 1,  $k$  is calculated at  $8.27 \times 10^{-3} \text{ W}/(\text{mK})$ , which is negligible compared with the thermal conductivity measured in our experiment. This shows that electrons have very weak contribution to thermal transport in CNTs compared with that from phonons.

For the thermal conductivity of CNTs, former researchers obtained relatively higher values. For example, Berber et al. [33] used equilibrium and non-equilibrium molecular dynamics simulations to obtain a thermal conductivity of  $6600 \text{ W}/(\text{mK})$ . Kim et al. [2] measured the SWCNT by a microfabricated device as  $3000 \text{ W}/(\text{mK})$ . Hone et al. [34] obtained the result for CNT film as  $200 \text{ W}/(\text{mK})$ . Our measured relatively low thermal conductivity is due to several physical reasons. First, compared with a single CNT, the CNT buckypaper have less heat transfer loss to the surroundings by thermal radiation [35]. For a single CNT sample, its extremely high surface to volume ratio will make the radiation heat transfer from the surface very important, leading to unreal-

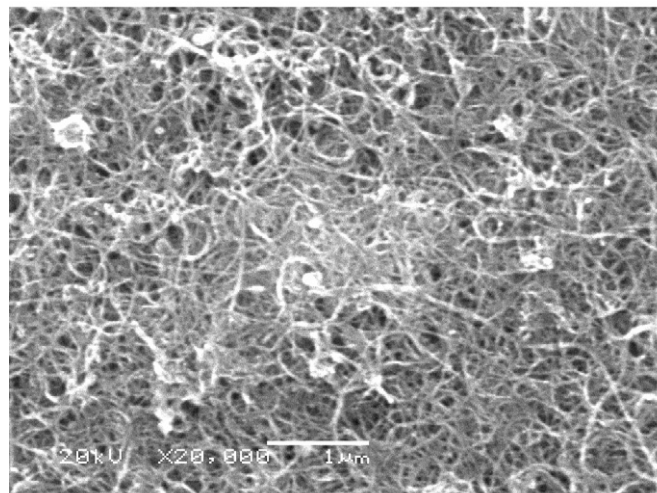


**Fig. 7.** The SEM image of buckypaper. The diameter of nanotubes is estimated as 30 nm.

istic high thermal conductivity. Second, the bulk CNT samples can have smaller thermal conductivity due to the intertube coupling [2, 33,36]. Chalopin et al. [37] computed the interface thermal resistance of the SWCNT and pointed out that the thermal conductivity of bulk CNT sample has the upper limit as low as  $5 \text{ W}/(\text{mK})$  for all chiralities. As shown in Fig. 7, the CNTs are bundled together disorderly in our buckypaper samples. Therefore, the thermal conductivity measured for buckypaper, which is smaller than the former researcher's results, is reasonable.

In fact, the heat conduction of the CNT buckypaper depends not only on the length of a single nanotube but also on the interface between different nanotubes. Chalopin et al. established an equation to describe the relationship between thermal conductivity and the sample density as  $k \approx 0.09\sigma \cdot l \cdot \rho / (\pi \cdot d \cdot \rho_{\text{graphene}})$  for single-wall CNT bundles, where  $\sigma$  is the interface conductance which is evaluated in their work using atomistic Green's function approach,  $l$  is the length of the tube between two adjacent contact points. When the tubes are not straight but bend like noodles,  $l$  is regarded as the curvature diameter.  $\rho_{\text{graphene}}$  is the surface mass density of graphene,  $\rho$  and  $d$  are the density of the bulk CNT and diameter of a single tube, respectively [37]. For the MWCNT buckypaper studied in this work, its thermal conductivity can be expressed as  $k \sim 2\sigma \cdot l \cdot \rho / [\pi \cdot (d_1^2 - d_2^2) \cdot \rho_g]$ , where  $d_1$  and  $d_2$  are the outer and inner wall diameters of the CNT, respectively.  $\rho_g$  is the volumetric density of graphene. This relation is based on the assumption that the thermal resistance of the CNT itself is much smaller than that of the contact between CNTs. Such assumption is physically reasonable due to the large thermal conductivity of CNTs reported.

The conductance of the sample varies with temperature and is different for various chiralities. In our experiment, the conductance can be regarded as constant because of the low range of temperature increase. In Chalopin's work, the thermal conductance of the CNT–CNT contact is computed as 10 to 100 pW/K for different chiralities [37]. As shown in Fig. 7 for the SEM image of the buckypaper, the tubes are intertwined with each other in a disorderly fashion. Based on our measurement results, assuming a 5 nm wall thickness of the MWCNTs, the mean distance between two adjacent tube contact points is estimated in the ranges of 45–450  $\mu\text{m}$  and 93–933  $\mu\text{m}$  for Samples 1 and 2, respectively. The thermal conductance of MWCNT of such length is about 873–8730 pW/K and 421–4210 pW/K based on an assumed thermal conductivity of MWCNT:  $1000 \text{ W}/(\text{mK})$ . This thermal conductance is much larger than that of the CNT contact point, meaning the thermal resistance

of the contact points is much larger than that of the CNT between two contact points.

Furthermore, the alignment of CNTs in the buckypaper will also affect its thermal transport properties. If the CNTs are tortuously bundled with each other, not rectilinearly distributed along the length direction of the specimen, the whole length of heat conduction would increase accordingly. Consequently, the thermal transport properties like the thermal conductivity of the bundle would decrease. As shown in Fig. 7 for the SEM image of the sample, the CNTs are not aligned very well. This is another important factor beside the high contact resistance leading to the low thermal conductivity of the sample.

### 3.4.2. Uncertainty induced by location of laser focal point

One possible uncertainty of the measurement comes from the shift of the laser focal point position from the middle point of the sample. In the physical model established above, the temperature is for the middle point of the sample. If the laser is not focused on that point, the measured temperature will deviate from the middle point one and give uncertainty in the final thermal conductivity evaluation. Assuming the position shift is  $\Delta r$ , the measured temperature should be between  $\dot{Q}_e(L + \Delta r)^2(T_L + \beta)/2\alpha + T_\infty$  and  $\dot{Q}_e(L - \Delta r)^2(T_L + \beta)/2\alpha + T_\infty$ , and it is reasonable to assume the temperature is the average of these two as  $\dot{Q}_e(L^2 + \Delta r^2)(T_L + \beta)/2\alpha + T_\infty$ . If we assume the position shift is 10% of the total sample length, we have  $\Delta r = 0.2L$ . In fact, this assumption represents the upper limit of uncertainty in the laser beam location. Our experiment is carefully controlled to be well within this position uncertainty arrange. This large position uncertainty (0.2L) will give only 4% uncertainty in the middle point temperature measurement. In conclusion, the uncertainty of the laser focal point position would have very limited effect on the accuracy of final thermal conductivity measurement.

### 3.4.3. Effect of thermal and electrical contact resistances and thermal transport in electrodes

In the physical model describing the heat transfer in the sample, we assume the connection point between the wire and the electrode stays at room temperature during the heating process. In fact, this assumption neglects three thermal transport effects: the effect of thermal contact resistance, effect of electrical contact resistance and heat transfer effect from the sample ends to the electrodes. All these effects would more or less affect the heat transfer process along the wire and give rise to some uncertainty. Taking all these effects into consideration, the real temperature of the endpoint is derived as:

$$T_L = \frac{P \cdot R_{tc}}{2} + \frac{I^2 R_c}{2D \cdot k_s} + \frac{P}{4D \cdot k_s} + T_\infty, \quad (7)$$

where  $R_{tc}$  is the thermal contact resistance per unit area,  $D$  the (effective) diameter of the sample,  $k_s$  the thermal conductivity of the electrode, and  $R_c$  the electrical contact resistance. In the above equation, the first three terms, from left to right, are temperature rises induced by the thermal contact resistance, the electrical contact resistance at the sample–electrode contact and the 3D heat transfer in the electrode. Accordingly, the measured middle point temperature can be revised to reflect all these effects as

$$T_m = \frac{P \cdot L}{4k \cdot A_c} + \frac{P \cdot R_{tc}}{2} + \frac{I^2 R_c}{2D \cdot k_s} + \frac{P}{4D \cdot k_s} + T_\infty. \quad (8)$$

In this equation, the term  $L/(k \cdot A_c)$  ( $k$  and  $A_c$  are the thermal conductivity and cross section area of the sample) is the thermal resistance of the sample of half length, and can be used as a sound reference for analysis. If  $R_{tc}$  is far smaller than  $L/(k \cdot A_c)$ , the effect of the thermal contact resistance will become negligible. In gen-

eral, the thermal contact resistance is around  $10^{-9}$ – $10^{-6}$  m<sup>2</sup> K/W. In our measurement, assuming the thermal contact resistance as  $10^{-6}$  m<sup>2</sup> K/W (the upper limit), the ratio of  $R_{tc}$  to  $L/(k \cdot A_c)$  is as low as  $5.26 \times 10^{-11}$  and  $3.76 \times 10^{-10}$  for Samples 1 and 2 respectively. Therefore, the thermal contact resistance will have negligible effect on the measurement results.

For the effect of electrical contact resistance, it can also be ignored when  $R_c/(2D \cdot k_s)$  is much smaller than  $R \cdot L/(4k \cdot A_c)$ . Their ratio  $2R_c \cdot k \cdot A_c/(D \cdot k_s \cdot R \cdot L)$  reflects two combined effect competitions: the competition between the electrical heating in the wire and that by the electrical contact resistance, and the competition between the thermal resistance of the wire and that of the electrode base. In our work, it has been observed that the electrical contact resistance is around or less than 0.13  $\Omega$  for a 25.4  $\mu$ m thick Pt wire when silver paste is applied at the contact point [5]. For the CNT samples measured in this work, they have larger contact area with the silver paste than the Pt wire, meaning a smaller electrical contact resistance is expected. Applying a contact resistance of 0.1  $\Omega$  and the thermal conductivity of copper as 401 W/(mK) [30], the ratio  $2R_c \cdot k \cdot A_c/(D \cdot k_s \cdot R \cdot L)$  is calculated as  $2.48 \times 10^{-6}$  and  $3.49 \times 10^{-5}$  for Samples 1 and 2. This indicates the electrical contact resistance effect can be neglected in our measurement.

The fourth term on the right side of Eq. (8):  $P/(4D \cdot k_s)$  reflects the effect of the 3D heat transfer in the electrode base with its thermal resistance of  $1/(2D \cdot k_s)$ . The ratio of this thermal resistance to that of the wire (half length) is expressed as  $k \cdot A_c/(D \cdot k_s \cdot L)$ , and is  $4.99 \times 10^{-4}$  and  $1.40 \times 10^{-3}$  for Samples 1 and 2, respectively. Consequently, the effect of the 3D heat transfer in the electrode base can be neglected and the temperature at the sample–base contact can be assumed room temperature.

As discussed above, successful application of the SERT technique is closely related to sample dimensions, electrode's thermal properties and connection points' thermal and electrical properties. Only when the thermal resistance and the electrical resistance of connection points are relatively small and the thermal conductivity of electrodes is much larger than that of the sample, the high accuracy of this technique can be assured. As a general rule, micro/nanowires with high  $L/A_c$  ratio are favorable in terms of reducing the effect of thermal and electrical contact resistances.

### 3.4.4. Extended application of SERT

In the SERT technology, the temperature of the sample is measured by the Raman spectroscopy. One natural extension would be to measure the sample's temperature based on its temperature-dependence of electrical resistance, which has been tested successfully in our laboratory using microscale Pt wires. It was found that the electrical contact resistance between the sample and electrodes could give undesired effect for samples of small intrinsic electrical resistance. This is because in calibration, the whole sample including the contact points are heated up to the same temperature while in the real thermal conductivity measurement, the contact points are usually at (or close to) room temperature when the sample is heated up by the electrical current. Such contact resistance effect would affect much more for this electrical resistance based method, sometimes would lead to failure of the measurement. In the measurement of this Raman based work, the middle point temperature of the sample is of the most concern. The electrical contact resistance affects less than the method above. For samples very short, see, much shorter than the focal point size of the probing laser, the SERT technique can be applied by measuring the average temperature of the sample using Eq. (5) instead of the middle point temperature. In this way, the SERT technique is applicable to measure the thermal conductivity of extremely short nanowires.

#### 4. Conclusion

In this work, the thermophysical properties of MWCNT buckypapers were characterized using the SERT technique combined with the TET technique. The thermal conductivity, thermal diffusivity, and density of two buckypapers were measured as 1.19 and 2.92 W/(mK),  $3.65 \times 10^{-6}$  and  $7.58 \times 10^{-6}$  m<sup>2</sup>/s, and 459 and 543 kg/m<sup>3</sup>, for Samples 1 and 2, respectively. The low thermal conductivity of the buckypaper is attributed to the tangled CNT structure and the low thermal conductance of the CNT–CNT contact. Such contact points dominate the thermal transport in the buckypapers. Based on the measurement result and the CNT size, the mean distance between two adjacent contact points was estimated in the order 45–450 μm and 93–933 μm for Samples 1 and 2, reflecting low-density contacts within the buckypaper.

#### Acknowledgement

Support of this work from NSF (CBET: 0931290) is gratefully acknowledged.

#### References

- [1] J. Hou, X. Wang, P. Velleacheruvu, J. Guo, C. Liu, H.-M. Cheng, *J. Appl. Phys.* 100 (2006) 124314.
- [2] P. Kim, L. Shi, A. Majumdar, P.L. McEuen, *Phys. Rev. Lett.* 87 (2001) 215502.
- [3] L. Shi, Q. Hao, C. Yu, N. Mingo, X. Kong, Z.L. Wang, *Appl. Phys. Lett.* 84 (2004) 2638.
- [4] J. Hou, X. Wang, L. Zhang, *Appl. Phys. Lett.* 89 (2006) 152504.
- [5] J. Guo, X. Wang, T. Wang, *J. Appl. Phys.* 101 (2007) 063537.
- [6] J. Guo, X. Wang, L. Zhang, T. Wang, *Appl. Phys. A* 89 (2007) 153.
- [7] T. Wang, X. Wang, J. Guo, Z. Luo, K. Ceng, *Appl. Phys. A* 87 (2007) 599.
- [8] J. Guo, X. Wang, D.B. Geohegan, G. Eres, C. Vincent, *J. Appl. Phys.* 103 (2008) 113505.
- [9] R. Tsu, J.G. Hernandez, *Appl. Phys. Lett.* 41 (1982) 1015.
- [10] F. Huang, K.T. Yue, P. Tan, S.-L. Zhang, Z. Shi, X. Zhou, Z. Gu, *J. Appl. Phys.* 84 (1998) 4022.
- [11] I.K. Hsu, R. Kumar, A. Bushmaker, S.B. Cronin, M.T. Pettes, L. Shi, T. Brintlinger, M.S. Fuhrer, J. Cumings, *Appl. Phys. Lett.* 92 (2008) 063119.
- [12] M. Freitag, Y. Martin, V. Perebeinos, Z. Chen, J.C. Tsang, P. Avouris, *Nano Lett.* 9 (2009) 1883.
- [13] E.F. Antunes, A.O. Lobo, E.J. Corat, V.J. Trava-Airoldi, A.A. Martin, C. Verissimo, *Carbon* 44 (2006) 2202.
- [14] S. Costa, E. Borowiak-Palen, M. Kruszyńska, A. Bachmatiuk, R.J. Kalenczuk, *Mater. Sci.* 26 (2008) 433.
- [15] Y. Zhang, L. Xie, J. Zhang, Z. Wu, Z. Liu, *J. Phys. Chem. C* 111 (2007) 14031.
- [16] L. Song, W. Ma, Y. Ren, W. Zhou, S. Xie, P. Tan, L. Sun, *Appl. Phys. Lett.* 92 (2008) 121905.
- [17] Z. Zhou, X. Dou, L. Ci, L. Song, D. Liu, Y. Gao, J. Wang, L. Liu, W. Zhou, S. Xie, D. Wan, *J. Phys. Chem. B* 110 (2006) 1206.
- [18] Q. Zhang, D.J. Yang, S.G. Wang, S.F. Yoon, J. Ahn, *Smart Mater. Struct.* 15 (2006) S1.
- [19] Z.H. Ni, H.M. Fan, X.F. Fan, H.M. Wang, Z. Zheng, Y.P. Feng, Y.H. Wu, Z.X. Shen, *J. Raman Spectrosc.* 38 (2007) 1449.
- [20] S. Chiashi, Y. Murakami, Y. Miyauchi, S. Maruyama, *Therm. Sci. Eng.* (2005) 71.
- [21] Y. Yue, G. Eres, Xinwei Wang, L. Guo, *Appl. Phys. A* (2009) 19.
- [22] N. Mingo, D.A. Broido, *Nano Lett.* 5 (2005) 1221.
- [23] G.E. Begtrup, *Phys. Rev. Lett.* 99 (2007) 155901.
- [24] E. Pop, *Phys. Rev. Lett.* 95 (2005) 155505.
- [25] T.J. Singh, *Phys. Rev. B* 25 (1982) 4106.
- [26] E. Pop, *Nano Lett.* 6 (2006) 96.
- [27] N. Mingo, *Phys. Rev. Lett.* 95 (2005) 96105.
- [28] K. Behler, S. Osswald, H. Ye, S. Dimovski, Y. Gogotsi, *J. Nanopart. Res.* 8 (2006) 615.
- [29] M.S. Dresselhaus, G. Dresselhaus, R. Saito, A. Jorio, *Phys. Rep.* 409 (2005) 47.
- [30] F.P. Incropera, D.P. Dewitt, T.L. Bergman, A.S. Lavine, *Fundamentals of Heat and Mass Transfer*, 6th ed., John Wiley & Sons, Inc., New York, 2007.
- [31] C. Kittel, *Introduction to Solid State Physics*, 8th ed., Wiley, New York, 2005.
- [32] J. Hone, M. Whitney, C. Piskoti, A. Zettl, *Phys. Rev. B* 59 (1999) R2514.
- [33] S. Berber, *Phys. Rev. Lett.* 84 (2000) 4613.
- [34] J. Hone, M.C. Llaguno, N.M. Nemes, A.T. Johnson, J.E. Fischer, D.A. Walters, M.J. Casavant, J. Schmidt, R.E. Smalley, *Appl. Phys. Lett.* (2000) 666.
- [35] D.J. Yang, *Phys. Rev. B* 66 (2002) 165440.
- [36] J. Che, T. Çagin, W.A. Goddard, *Nanotech.* (2000) 65.
- [37] Y. Chalopin, S. Volz, N. Mingo, *J. Appl. Phys.* (2009) 084301.